

# Mechanical Properties and Microstructures of Commercial-Purity Aluminum Processed by Rotational Accelerated Shot Peening Plus Cold Rolling

Yanfang Liu, Yang Cao, Hao Zhou, Xuefei Chen, Ying Liu,\* Lirong Xiao,\* Xiaowei Huan, Yonghao Zhao, and Yuntian Zhu

Commercial-purity aluminum with 99.7% purity is processed by rotational accelerated shot peening (RASP) and cold-rolling. RASP samples are rolled at room temperature to a thickness reduction of 20% and 30%, for the purpose of surface roughness reduction and strengthening. Detailed microstructural characterization and hardness tests reveal that cold-rolling cause grain growth at the surfaces of RASP samples from  $\approx 472$  to  $\approx 1000$  nm. Moderate cold-rolling is effective in smoothing the surface of RASP samples, while improving strength and maintaining ductility. However, cold-rolling to more than 30% thickness reduction eventually diminishes the gradient nanostructure. During cold-rolling of RASP samples, a transition zone with strong strain incompatibility is noticed by a sharp rise in hardness at some point of the hardness-distribution curve from the surface to the core of the sample. This transition zone is a result of quick generation of geometrically necessary dislocations. Although the transition zone with strong strain incompatibility is short-lived, it is anticipated to be common among gradient-nanostructured materials under cold-rolling condition.

nanostructured materials is often limited to a few percent due to suppressed dislocation activities and temperature-sensitive grain boundary activities.<sup>[5–8]</sup> Inspired by the architectures of natural structural materials such as bamboos, seashells, and mammal's teeth, which usually embrace gradient structures,<sup>[9–11]</sup> researchers could eventually unite the superior strength and excellent ductility in a single-phase material by introducing gradient nanostructures.<sup>[9,10]</sup>

To date, surface nano-crystallization (SNC) techniques including surface mechanical attrition treatment (SMAT),<sup>[12–15]</sup> surface mechanical grinding treatment (SMGT),<sup>[16]</sup> and surface mechanical rolling treatment (SMRT)<sup>[17]</sup> are common practice for processing materials with gradient nanostructures. The aforementioned SNC techniques make gradient nanostructures by imposing severe plastic deformation to the surface

of experimental materials. Depending on the intrinsic properties of materials such as stacking fault energy (SFE), melting temperature and short-range ordering, and the external processing conditions such as force, strain rate, and temperature, various deformation mechanisms including dislocation slip, deformation twinning, grain boundary sliding, and grain rotation may be activated to facilitate the formation of the gradient nanostructures in the materials.<sup>[18–23]</sup> Thus, the microstructures of SNC-treated materials may vary due to different processing conditions, and the effects of each SNC technique on mechanical properties of different materials may also be very different.

After more than 10 years extensive research in the field of SNC-processing gradient-nanostructured materials, many interesting results have been obtained. To date, gradient nanostructures have been made in many materials including steels,<sup>[11,17,24,25]</sup> pure Cu,<sup>[10]</sup> pure Fe,<sup>[26]</sup> and Mg alloys,<sup>[27,28]</sup> and it was found that only Cu with gradient nanostructures tend to break the trend of the “strength-ductility banana curve” (significantly increase in strength while keeping the ductility nearly unchanged).<sup>[10]</sup> The outstanding mechanical properties of Cu with gradient nanostructures are attributed to the sufficiently active stress-driven grain growth which occur in the nanostructured surface layers, and the resulting concurrently uniform deformation in both nanostructured surface layers and the coarse-grained core. In contrast, for an interstitial free (IF)-steel

## 1. Introduction

In the last 30 years, dramatic progress has been achieved in processing nanostructured metallic materials that usually exhibit superior strength in contrast to their coarse-grained counterparts.<sup>[1–4]</sup> However, it is also realized that the ductility of homogeneously

Dr. Y. Liu, Dr. Y. Cao, Dr. H. Zhou, Dr. Y. Liu, Dr. L. Xiao, Dr. X. Huan, Dr. Y. Zhao, Dr. Y. Zhu  
Nano and Heterogeneous Materials Center  
School of Materials Science and Engineering  
Nanjing University of Science and Technology  
Nanjing 210094, P. R. China  
E-mail: liuying517@njust.edu.cn; xiaolr620@njust.edu.cn

Dr. X. Chen  
State Key Laboratory of Nonlinear Mechanics  
Institute of Mechanics  
Chinese Academy of Sciences  
Beijing 100190, China

Dr. Y. Zhu  
Department of Materials Science and Engineering  
North Carolina State University  
Raleigh, NC 27695, USA

 The ORCID identification number(s) for the author(s) of this article can be found under <https://doi.org/10.1002/adem.201900478>.

DOI: 10.1002/adem.201900478

with gradient nanostructures, strong strain gradients and changes in stress state are observed between nanostructured layers and the coarse-grained core. As a result, although the tensile ductility of the gradient-nanostructured IF-steel was lower than the coarse-grained counterparts, an interesting upturn of strain hardening rate was evident during the tensile test. Clearly, the mechanical properties of SNC-treated materials have to be optimized by careful manipulation of the processing conditions with respect to the intrinsic properties of experimental materials.

Recently, a new SNC technique has been developed, by which gradient nanostructures are made by rotational accelerated shot peening (RASP).<sup>[29]</sup> RASP technique is similar to SMAT technique; the difference lies in the way of generating momentum to the shots (metallic balls). Readers are referred to literature for more details on RASP.<sup>[29–32]</sup> During RASP treatment, spherical shots continuously impact on the surfaces of a sample material, resulting in hardened rough surfaces. Although, it has been experimentally shown that surface roughness created by SMAT and RASP only poses limited effects on the mechanical properties of the materials, sometimes it is still ideal to smooth the surface of SNC-treated materials.<sup>[11]</sup> Therefore, moderate cold-rolling after SMAT or RASP is often used to reduce the surface roughness while maintaining the gradient nanostructures.

Aluminum and its alloys are commonly used materials in nearly all aspects of human life. They represent a class of metallic materials with high SFEs and prone to dynamic recovery at reduced grain sizes. For the purposes of expanding the application of RASP methods and in-depth understanding of the mechanical behaviors of Al alloys, a systematic analysis was performed on a model material. The effect of RASP and subsequent cold-rolling on microstructures and mechanical properties are investigated in detail in seeking both unique and common phenomenon associated with plastic deformation of gradient-nanostructured materials.

## 2. Results

As shown in **Figure 1a**, gradient grain size distribution is apparent from the RASP sample surface toward the interior. **Figure 1d** is a high-magnification image showing the rough and slightly damaged surface of the RASP sample. In the RASP + Roll20% samples, gradient grain size is still observable, as shown in **Figure 1b,e**. The sample surface shown in **Figure 1b** is very smooth compared with the RASP sample shown in **Figure 1a**. The grains away from the sample surface are slightly elongated along the rolling direction. When a RASP sample was further rolled to 30% thickness reduction, the surface layer with fine grain structures became much thinner than that in RASP and RASP + Roll20% samples, as shown in **Figure 1c,f**. However, the smoothness of the RASP + Roll30% sample surface (**Figure 1c**) was just comparable to the RASP + Roll20% sample surface (**Figure 1b**). Thus, it is clear that cold-rolling to 20% thickness reduction is almost the optimum processing condition for improving the surface smoothness of the RASP commercial-purity aluminum (CP-Al) samples while keeping nanostructured surface layers.

Electron backscatter diffraction (EBSD) analysis was conducted to quantitatively and qualitatively investigate the microstructures of samples processed by different routes. In **Figure 2**, the grain structures, grain orientations, high-angle grain boundaries (HAGBs,  $>15^\circ$ ) and low-angle grain boundaries (LAGBs,  $3\text{--}15^\circ$ ) are clearly shown. **Figure 2a–c** show the microstructures near surfaces of the RASP, RASP + Roll20%, and RASP + Roll30% samples, respectively. At the very surface of the samples, the EBSD detection rate was comparatively low due to ultrafine structures and high densities of defects. The RASP sample had a surface roughness of  $\approx 200\ \mu\text{m}$ , thus it was difficult to accurately measure the thickness of surface layers containing severely deformed structures by EBSD. Once the surface roughness was significantly reduced by rolling to 20% and

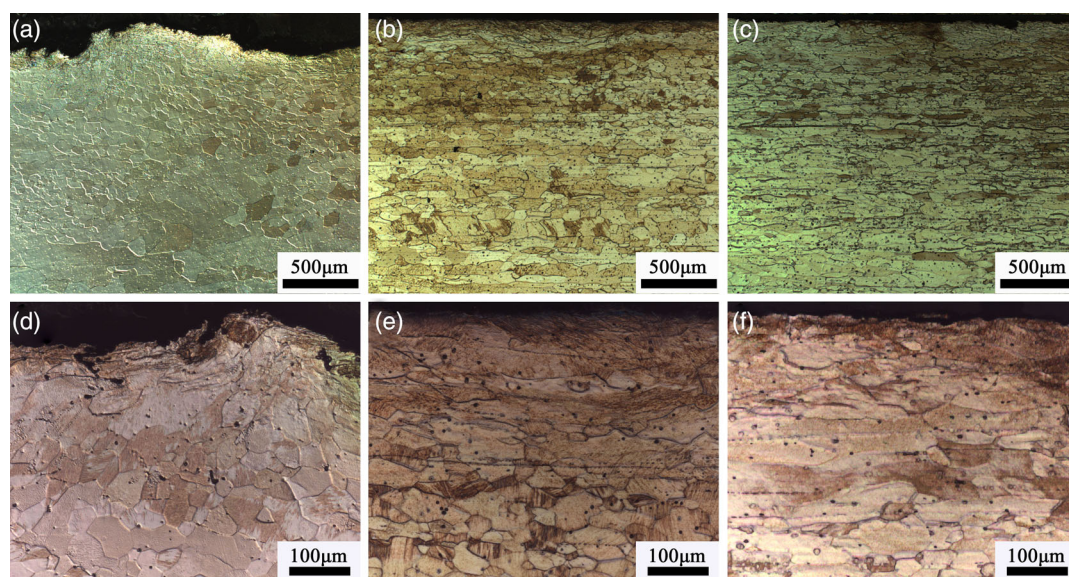


**Figure 1.** Optical microscopy images showing cross-sectional microstructures near the surfaces of the samples processed by a,d) RASP, b,e) RASP + Roll20%, and, c,f) RASP + Roll30%

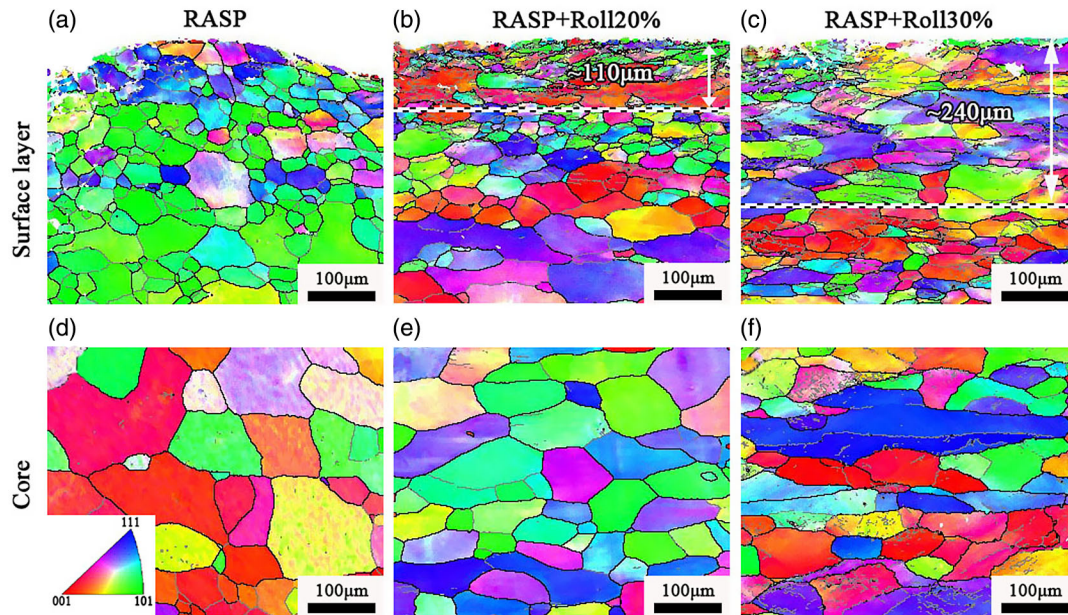


**Figure 2.** EBSD images showing cross-sectional microstructures of the samples processed by a,d) RASP, b,e) RASP + Roll20%, c,f) RASP + Roll30%. a–c) were obtained near the surfaces of the samples, d–f) were obtained at core regions of the samples. (HAGBs and LAGBs are traced in black and gray colors, respectively. The color code used in the images is inserted in d)).

30% thickness reduction, the thicknesses of severely deformed surface layers in RASP + Roll20% and RASP+Roll30% samples were  $\approx 110$  and  $240 \mu\text{m}$ , respectively. At the core of the RASP sample, grains were equiaxed and the dislocation density was low. It is clear that RASP processing under current condition did not induce deformation to the core of the CP-Al sample plate with a thickness of 4 mm. Therefore, the elongated grains and increased dislocation densities at the cores of the RASP + Roll20% and RASP + Roll30% samples were results of cold-rolling, as shown in Figure 2e,f.

Distributions of misorientation angles for RASP, RASP + Roll20%, and RASP + Roll30% samples are shown in Figure 3. Despite the limited detection rate of EBSD on the surfaces of RASP samples, the fraction of LAGBs was  $\approx 50.5\%$ . This is clearly lower than the fractions of LAGBs at the surfaces of RASP + Roll20% and RASP + Roll30% samples, which are 64.3% and 72.7%, respectively. The fractions of LAGBs at the cores of the RASP, RASP + Roll20%, and RASP + Roll30% samples were 26.2%, 49.7%, and 69.5%, respectively. The increase in the fraction of LAGBs was attributed to the cold-rolling process, which is effective in increasing the dislocation density in coarse-grained materials.<sup>[5,33,34]</sup>

To reveal the microstructures of the topmost surface layers, which are the most important features of SNC-processed materials, high-resolution EBSD was conducted on small areas adjacent to the surfaces as shown in Figure 4. The EBSD detection rates for Figure 4a–c are 74%, 77%, and 82%, respectively. It can be clearly seen from Figure 4, that within  $20 \mu\text{m}$  of the top surface layers, the RASP sample (Figure 4a) has more well-developed ultrafine grains than RASP + Roll20% (Figure 4b) and RASP + Roll30% (Figure 4c) samples. This result indicates that cold-rolling somehow reduced the fractions of equiaxed ultrafine grains.

Although the EBSD detection rates have been well controlled above 70% for each image taken, the actual detection rates at nanostructured layers are lower than 70%. To reveal the detailed microstructures that might be missed by the EBSD analysis, extensive transmission electron microscopy (TEM) analysis was conducted purposely to investigate the microstructures within  $10 \mu\text{m}$  beneath the surface. Substantial grain refinement at the surfaces of the samples was achieved by RASP as shown in Figure 5a and the diffraction rings in the inset. The majority of the grains are equiaxed, with an average grain size of  $\approx 472 \text{ nm}$ , as shown in Figure 5d. Interestingly, the shapes and sizes of the grains at the surfaces of the RASP + Roll20% (Figure 5b) and RASP + Roll30% (Figure 5c) samples are significantly different from the RASP sample. The inserted diffraction patterns with arced diffraction spots in Figure 5b,c indicate that the elongated grains were distorted by dislocation substructures. The average width of the grains is about  $990 \text{ nm}$ , and the average length is about  $2748 \text{ nm}$  at the surface of the RASP + Roll20% sample (Figure 5e). The average width of the grains is about  $1026 \text{ nm}$ , and the average length is about  $2880 \text{ nm}$  at the surface of the RASP + Roll30% sample (Figure 5f). It is difficult at the current stage to determine the actual mechanism for the apparent grain growth. Notwithstanding, it is clear that cold-rolling to 20% thickness reduction is sufficiently effective in restructuring the grains at the RASP sample surface, thus achieving desired reduction of surface roughness.

The strength and hardness of metallic materials are related to the grain size as described by the famous empirical Hall–Petch relationship.<sup>[5,35]</sup> Therefore, hardness distribution from the surface to the core of a SNC-processed sample provides important information about the strength and the microstructural gradient. As summarized in Figure 6a, after RASP treatment, the

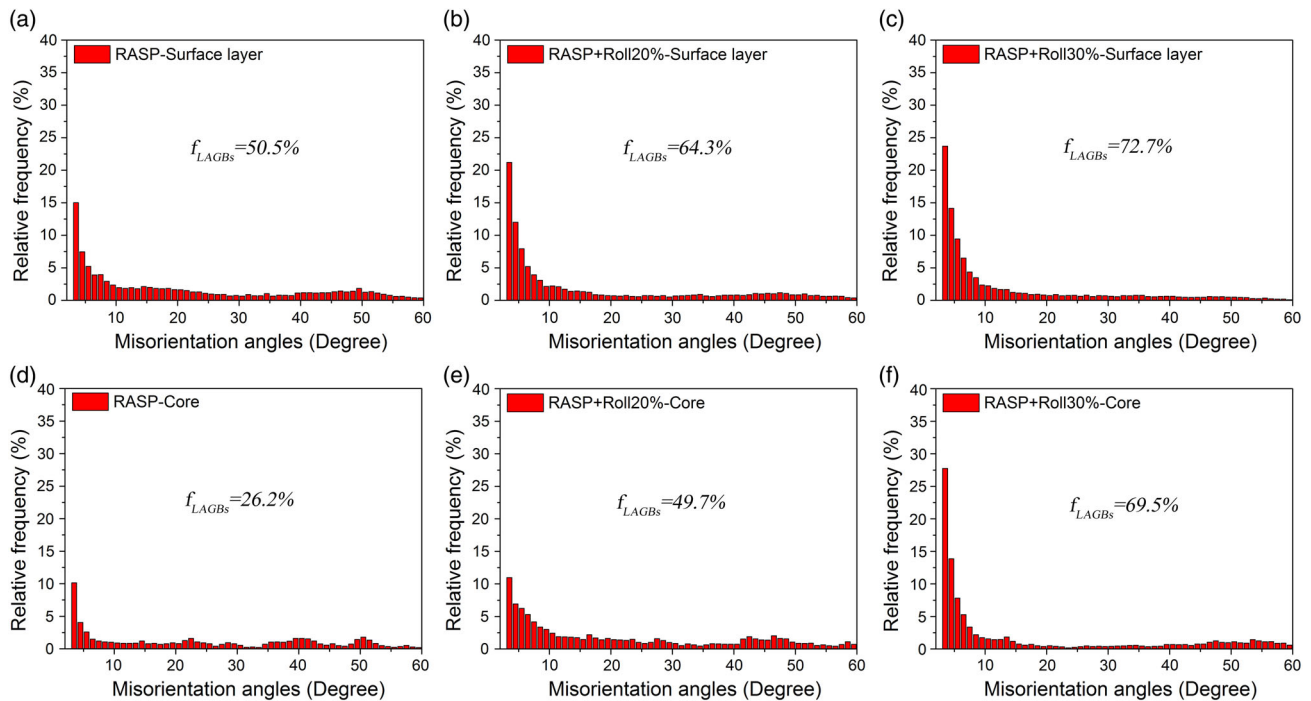


**Figure 3.** Distributions of misorientation angles at selected regions of the samples processed by a,d) RASP, b,e) RASP + Roll20%, and, c,f) RASP + Roll30%. a–c) were obtained near the surfaces of the samples, d–f) were obtained at core regions of the samples.

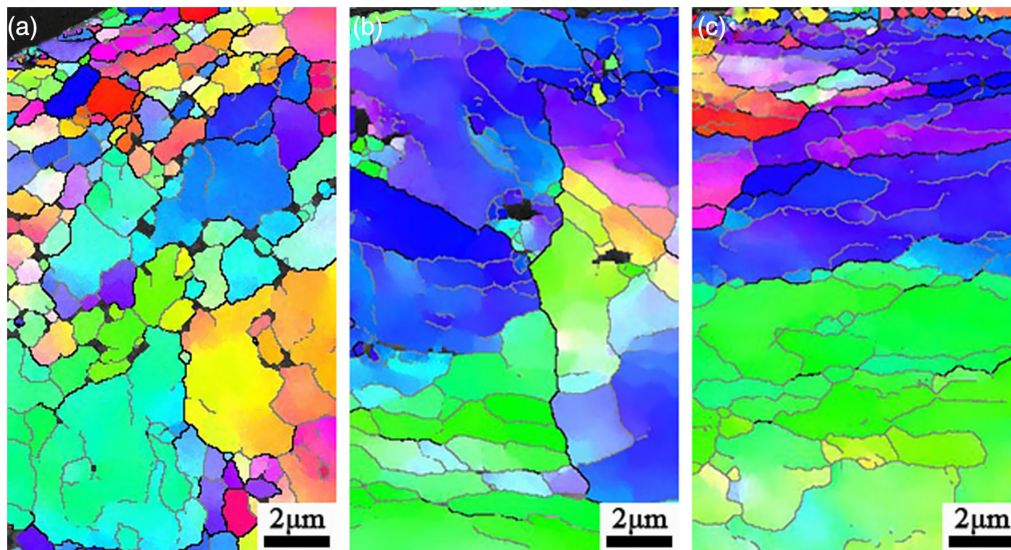


**Figure 4.** High-magnification EBSD images showing the microstructures at topmost surface of the samples processed by a) RASP, b) RASP + Roll20%, and c) RASP + Roll30%. (HAGBs and LAGBs are traced in black and gray colors, respectively.)

hardness at the topmost surface increased to 38.1 Hv, which is 78% higher than the core. Subsequent cold-rolling to thickness reductions of 20% and 30%, the hardness of surface layers decreased slightly to 36.0 and 32.7 Hv, respectively. In contrast, hardness at the cores of RASP + Roll20% and RASP + Roll30% samples are obviously higher than that of the RASP sample. Interestingly, the hardness distribution from the surface to

the core in the RASP+Roll20% sample shows significant undulation, which will be discussed later.

Figure 6b compares the effects of different processing conditions on mechanical properties of CP-Al. RASP, cold-rolling, and the combined method are effective in improving the yield strength (YS) of the CP-Al, at the expense of reducing uniform elongation (UE). After RASP processing, the YS and UE reaches

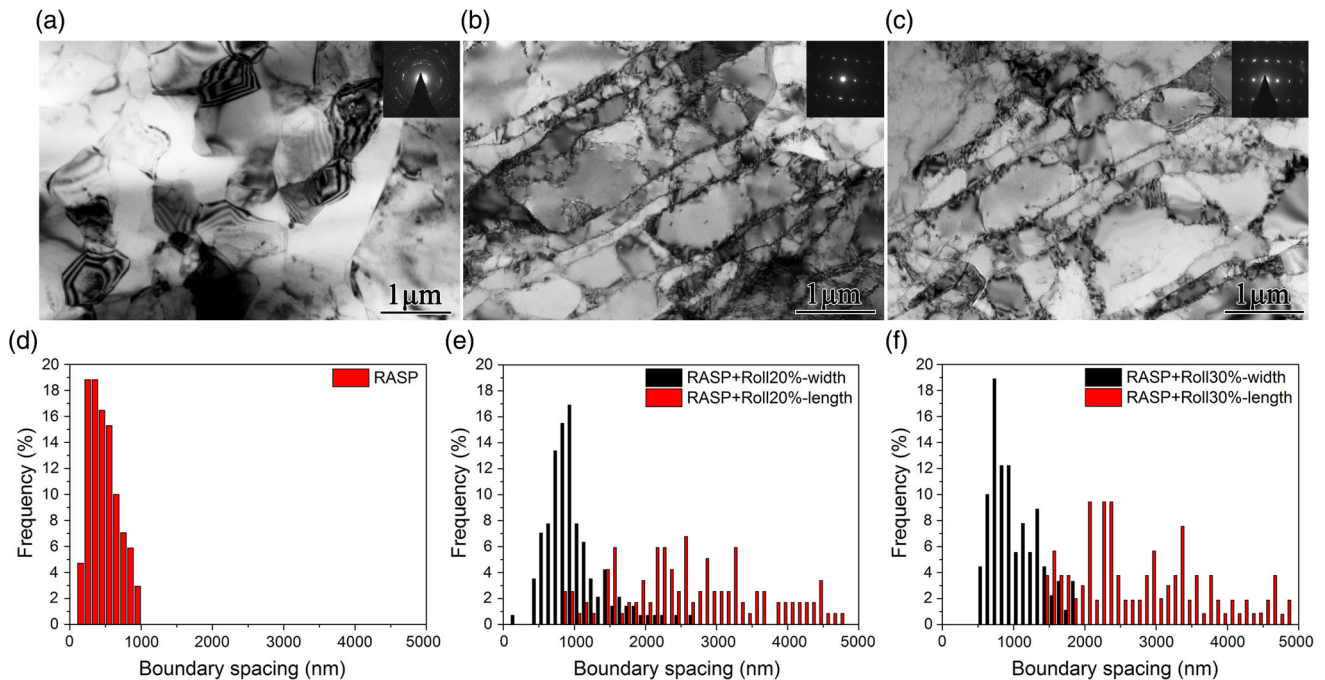


**Figure 5.** a–c) Typical TEM images showing the microstructures within  $\approx 10 \mu\text{m}$  beneath surfaces of the samples. d–f) Charts showing the grain size distributions at the surfaces of the samples. The samples were processed by a,d) RASP, b,e) RASP + Roll20%, and c,f) RASP + Roll30%.

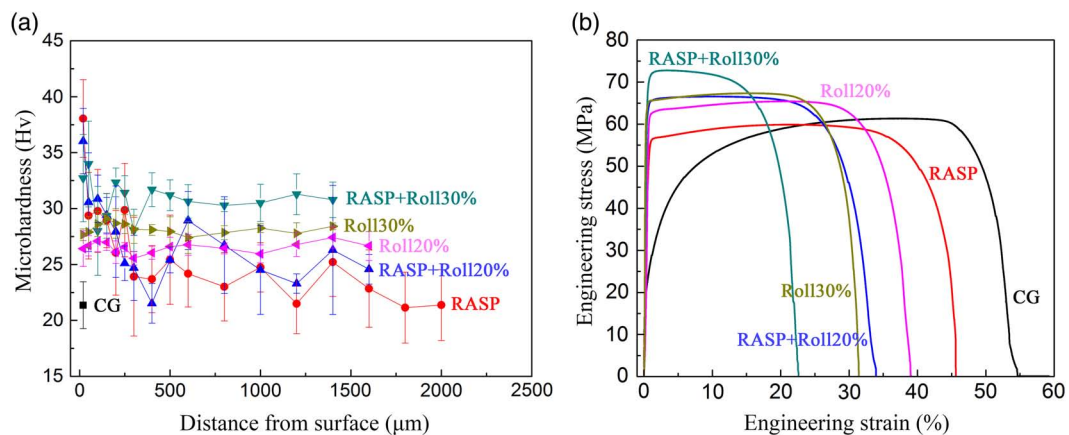


**Figure 6.** a) Hardness distributions from the surfaces to the cores of the samples; b) Engineering stress–strain curves of the samples.

56.3 MPa and 23.0%, respectively. The RASP + Roll20% sample exhibits a YS of 65.4 MPa and an UE of 13.1%. The RASP + Roll30% sample shows the highest YS of 72.1 MPa and the worst UE of 4.4%. For the purpose of comparison, tensile properties of cold-rolled samples were also plotted on Figure 6b. The sample rolled to 20% thickness reduction (curve Roll20% in Figure 6b) exhibits a YS of 62.3 MPa and an UE of 22.5%. The sample rolled to 30% thickness reduction (curve Roll30% in Figure 6b) exhibits a YS of 65.6 MPa and an UE of 17.7%. The YS of the RASP + Roll20% and the Roll30% samples are almost the same, whereas the UE of the RASP + Roll20% sample is smaller.

### 3. Discussion

CP-Al has some unique intrinsic properties such as high SFE and low melting temperature. Therefore, compared with many materials with low SFEs, strain-induced grain refinement is limited in CP-Al, and ultrafine-grained CP-Al are prone to dynamic recovery and even grain growth.<sup>[36,37]</sup> Provided that the initial grain sizes in the annealed sample were in the range of 50–120 μm, an average grain size of  $\approx 472 \text{ nm}$  in the surface layers of RASP samples represents significant grain refinement.<sup>[38]</sup> Literature state that the initial grain size may have a strong effect on the microstructures and textures evolutions during severe

plastic deformation. However, this effect only becomes noticeable when the initial grain sizes have more than tenfold differences.<sup>[39]</sup> Moreover, as the shear strain increases to a very high level, the effect of initial grain size on the microstructural evolution diminishes.<sup>[1,40]</sup> In the current case, the initial grain size does not vary significantly, thus the final ultrafine-grained structures at the surface of RASP samples were nearly unaffected by the initial coarse grain sizes.

In the current study, strain-induced grain-coarsening was observed when RASP samples were subsequently cold-rolled, as shown in Figure 2 and 4, and 5. There are three possible mechanisms that may contribute to the observed grain-coarsening phenomenon: 1) during cold-rolling, the ultrafine grains on the surface of the RASP sample could be squeezed in between the larger grains beneath; 2) shear stress and moderate heating during rolling may induce grain growth to the ultrafine grains;<sup>[41,42]</sup> 3) the fine grains with sizes of only a few micrometers may be refined into finer grains.<sup>[43]</sup> As shown in Figure 5a,d, the average grain size in the topmost surface of RASP sample was  $\approx 472$  nm; the average grain widths in the topmost surfaces of RASP + Roll20% (Figure 5e) and RASP + Roll30% (Figure 5f) samples were  $\approx 990$  and  $\approx 1026$  nm, respectively. The phenomenon of equiaxed ultrafine Al grains growing from 500 nm to 1000 nm under stress is similar to that under raising temperature. Likewise, sufficient strain input was necessary.<sup>[36,37,41]</sup> In contrast, it was impossible for large Al grains of a few tens of micrometers in size to deform into fine grains with a width of  $\approx 1000$  nm under a rolling strain of 0.26 (20% thickness reduction in the current case).<sup>[34,44]</sup> However, there are sufficient amount of fine grains located just beneath the ultrafine grains in the surfaces of RASP sample, and they can possibly be refined by dislocation structures as shown in Figure 5b,c. Considering the fact that the shear strains associated with 20% and 30% thickness reduction are small, significant grain growth or grain refinement are not feasible. Therefore, it is concluded that grain-coarsening occurred at the surface of the RASP samples during cold-rolling is a combined effect of the aforementioned mechanisms.

Clearly, Both RASP and cold-rolling are effective in strengthening CP-Al. It is difficult to tell which processing method is better in terms of optimizing the mechanical properties of CP-Al. Although RASP caused significant increase in surface roughness, the rough surface did not lead to any obvious local stress concentration or premature failure of the material. However, RASP + Roll30% sample exhibited quick necking and failure at only 4.4% UE. By examining the microstructures of the materials' surfaces, as shown in Figure 4, it can be seen that the microstructures at the surfaces of RASP and RASP + Roll20% samples are homogeneous, but the microstructures at the surface of the RASP + Roll30% sample are inhomogeneous. Although Figure 2c still show microstructural gradient from the surface to the interior in the RASP + Roll30% sample, the corresponding hardness gradient is very small, as shown in Figure 6a. The core region of the RASP + Roll30% sample has been strain-hardened significantly by cold-rolling. Therefore, the core region of the RASP + Roll30% sample has much less strain-hardening capacity than other samples with less deformed cores. According to literature and current

experimental results, there are two important factors contributing to the ductility of gradient-structured materials: 1) the surface layers with homogeneous ultrafine-grained structures can help in suppressing strain localization;<sup>[10,45]</sup> 2) Coarse-grained cores with minimal defect content provide large strain-hardening capacity to enhance ductility.<sup>[11,46]</sup>

As shown in Figure 6a, when the RASP sample was rolled to 20% thickness reduction, the hardness values decreased from surface to the core in an clear undulating manner. There was a sharp rise in hardness from 21.5 to 28.9 Hv from the depth of 400 to 600  $\mu\text{m}$ . The peak hardness value of 28.9 Hv was still lower than the average hardness of 30.9 Hv at the core region of the RASP + Roll30% sample. Thus, the undulating hardness distribution was attributed to the inhomogeneous strain-hardening effect which occurred during cold-rolling of the RASP sample. The gradient grain structures in the RASP sample led to strain gradient during cold-rolling process; the highest strain incompatibility should exist at the transition zone between hard ultrafine-grained layers and coarse-grained core regions. To accommodate the strain incompatibility, an increased amount of geometrically necessary dislocations would be created in the transition zone.<sup>[47-49]</sup> In the current study, the transition zone was located at  $\approx 600$  nm beneath the surface of the RASP sample, thus a sharp rise in hardness occurred at that location. It is anticipated that the transition zone with strong strain incompatibility was very short-lived, as evidenced by the hardness plateau of the RASP + Roll30% sample. Therefore, careful and detailed experiment is necessary for identifying the transition zone during the cold-rolling of any gradient nanostructured materials.

Strain incompatibility and the resulting hardness-transition zone are common intrinsic characteristics of gradient-structured materials.<sup>[11,48]</sup> Similar transition zone has also been observed in a gradient-nanostructured IF steel.<sup>[11]</sup> Interestingly, the transition zone was created during tensile deformation of the gradient-nanostructured IF steel. During tensile loading, the global loading stress is a simple uniaxial tensile stress parallel to the nanostructured surface layer of the IF steel. However, during cold-rolling, the global loading stress is a compressive stress normal to the nanostructured surface layer of the CP-Al in current study. Although the global loading stresses are different between the two studies, the local stress states at the transition zones are similar. During tensile loading of the gradient-nanostructured IF steel, the mutual constraint between the nanostructured surface layers and the coarse-grained core creates lateral stresses in the transition zone. In contrast, during cold-rolling of the gradient-nanostructured CP-Al, the global compressive stress is converted into a shear stress that consists of lateral stress components and vertical stress components. Despite the different loading modes, both materials show extra strain hardening at the transition zone, which is clearly attributed to the three-dimensional stress states at the local region and the resulting quick generation of additional amounts of geometrically necessary dislocations.

## 4. Conclusions

CP-Al samples were processed by RASP and subsequent cold-rolling. The microstructures, hardness, and stress-strain

relationship of processed materials were studied in detail. In summary, the following conclusions are drawn: 1) RASP technique is effective in creating gradient nanostructures in CP-Al. The average grain size within 10  $\mu\text{m}$  of the topmost surface of RASP sample was  $\approx 472$  nm. Subsequent cold-rolling to the RASP sample led to grain coarsening from  $\approx 472$  to  $\approx 1000$  nm at the surface layers. 2) An interesting transition zone with strong strain incompatibility was found in the RASP + Roll20% sample. The strain-hardening effect was significantly higher at the transition zone than adjacent regions. However, the transition zone was short-lived, and it quickly diminished with increasing rolling strain to 30% thickness reduction. It is anticipated that the transition zone was a result of quick generation of geometrically necessary dislocations in accommodating the strong local strain incompatibility. This transition zone can be common among many gradient-nanostructured materials under cold-rolling and/or similar deformation conditions.

## 5. Experimental Section

The material used in this investigation was a CP-Al with a purity of 99.7%, in the form of rectangular plates. The sample plate was annealed at 693 K for 1 h to obtain a homogeneous coarse-grained structure. The sizes of grains in the annealed sample were in the range of 50–120  $\mu\text{m}$ . The annealed samples were cut into small plates with dimensions of 4  $\times$  90  $\times$  110 mm. Each plate was processed by RASP at room temperature for 5 min, using GCr15 bearing steel balls with a diameter of 2 mm and a velocity of 40  $\text{m s}^{-1}$ . The RASP-processed samples were sorted into three batches. The first batch of the samples was directly used for mechanical properties tests, and this batch of samples was named “RASP sample” throughout this study. The second and third batch of samples were subsequently cold-rolled to 20% and 30% thickness reduction at room temperature, respectively. The second and third batch of samples were named “RASP + Roll20%” and “RASP + Roll30%” throughout this study, respectively. The processing parameters used in RASP and subsequent cold-rolling were chosen for optimized results on roughness and mechanical properties, based on a series of carefully designed trials. For the purpose of comparison, another two batches of samples were cold-rolled to 20% and 30% thickness reduction, and named “Roll20%” and “Roll30%”, respectively.

Laser scanning confocal microscopy (LSCM) analysis, EBSD analysis, and TEM analysis have been conducted to characterize the microstructures of the samples in detail. The samples for LSCM analysis were mechanically polished with 600, 800, and 1200 grit emery papers, then fine polished to mirror finish with diamond paste, and finally anodic coated in a solution of 40% fluoroboric acid with 20 V DC current. Samples for EBSD analysis were prepared by mechanical polishing and subsequent electrolytic polishing (10%  $\text{HClO}_4$  in alcohol, with 20 V and at 0  $^\circ\text{C}$ ). TEM samples were prepared by mechanical grinding to a thickness of 40  $\mu\text{m}$  and then ion beam thinned to perforation. TEM analysis was conducted on a Tecnai G20 S-TWIN TEM at an accelerating voltage of 200 keV.

Hardness tests were conducted on the polished cross-sections of the samples, with an HMV-G21 Vickers hardness tester at a load of 98.07 mN. The samples for tensile tests were cut to a gauge dimension of 25  $\times$  6  $\times$  4 mm. The tensile tests were performed at room temperature, using an AGS-X10KN tensile testing machine operating at a constant strain rate of  $5.6 \times 10^{-4} \text{ s}^{-1}$ .

## Acknowledgements

This work was supported by the National Key R&D Program of China (2017YFA0204403), National Natural Science Foundation of China

(51601094 [Y.C.]), the Fundamental Research Funds for the Central Universities (30918011342 [H.Z.] and 30919011412 [Y.Z.]) and the Open Research Fund of Science and Technology on High Strength Structural Materials Laboratory (Grant No. O2016006). The authors are grateful for the technical support from the Jiangsu Key Laboratory of Advanced Micro & Nano Materials and Technology, and the Materials Characterization Facility of Nanjing University of Science and Technology.

## Conflict of Interest

The authors declare no conflict of interest.

## Keywords

commercial-purity aluminum, gradient structures, mechanical properties, microstructures, plastic deformation

Received: April 30, 2019

Revised: June 14, 2019

Published online: August 8, 2019

- [1] A. P. Zhilyaev, T. G. Langdon, *Prog. Mater. Sci.* **2008**, *53*, 893.
- [2] T. G. Langdon, *Acta Metall. Mater.* **1994**, *42*, 2437.
- [3] H. Yi, T. G. Langdon, *Mater. Today* **2013**, *16*, 85.
- [4] Y. T. Zhu, X. Liao, *Nat. Mater.* **2004**, *3*, 351.
- [5] Y. Cao, S. Ni, X. Liao, M. Song, Y. Zhu, *Mater. Sci. Eng. R* **2018**, *133*, 1.
- [6] I. A. Ovid'ko, R. Z. Valiev, Y. T. Zhu, *Prog. Mater. Sci.* **2018**, *94*, 462.
- [7] X. Huang, N. Hansen, N. Tsuji, *Science* **2006**, *312*, 249.
- [8] Z. Shan, E. A. Stach, J. M. K. Wiezorek, J. A. Knapp, D. M. Follstaedt, S. X. Mao, *Science* **2004**, *305*, 654.
- [9] Z. Cheng, H. Zhou, Q. Lu, H. Gao, L. Lu, *Science* **2018**, *362*, 1925.
- [10] T. H. Fang, W. L. Li, N. R. Tao, K. Lu, *Science* **2011**, *331*, 1587.
- [11] X. Wu, P. Jiang, L. Chen, F. Yuan, Y. T. Zhu, *Proc. Natl. Acad. Sci.* **2014**, *111*, 7197.
- [12] K. Lu, J. Lu, *Mater. Sci. Eng. A* **2004**, *375–377*, 38.
- [13] Y. M. Wang, K. Wang, D. Pan, K. Lu, K. J. Hemker, E. Ma, *Scr. Mater.* **2003**, *48*, 1581.
- [14] K. Y. Zhu, A. Vassel, F. Brisset, K. Lu, J. Lu, *Acta Mater.* **2004**, *52*, 4101.
- [15] Z. B. Wang, J. Lu, K. Lu, *Surf. Coat. Technol.* **2006**, *201*, 2796.
- [16] W. L. Li, N. R. Tao, K. Lu, *Scr. Mater.* **2008**, *59*, 546.
- [17] T. Roland, D. Rehrig, K. Lu, J. Lu, *Scr. Mater.* **2006**, *54*, 1949.
- [18] F. Dalla Torre, R. Lapovok, J. Sandlin, P. F. Thomson, C. H. J. Davies, E. V. Pereloma, *Acta Mater.* **2004**, *52*, 4819.
- [19] Z. Horita, T. Fujinami, M. Nemoto, T. G. Langdon, *Metall. Mater. Trans. A* **2000**, *31*, 691.
- [20] S. Ni, Y. B. Wang, X. Z. Liao, S. N. Alhajeri, H. Q. Li, Y. H. Zhao, E. J. Lavernia, S. P. Ringer, T. G. Langdon, Y. T. Zhu, *Mater. Sci. Eng. A* **2011**, *528*, 3398.
- [21] M. Jin, A. M. Minor, E. A. Stach, J. W. Morris, *Acta Mater.* **2004**, *52*, 5381.
- [22] T. H. Fang, N. R. Tao, K. Lu, *Scr. Mater.* **2014**, *77*, 17.
- [23] Y. T. Zhu, T. G. Langdon, *JOM* **2004**, *56*, 58.
- [24] M. Yang, Y. Pan, F. Yuan, Y. Zhu, X. Wu, *Mater. Res. Lett.* **2016**, *4*, 145.
- [25] H. W. Zhang, Z. K. Hei, G. Liu, J. Lu, K. Lu, *Acta Mater.* **2003**, *51*, 1871.
- [26] N. R. Tao, Z. B. Wang, W. P. Tong, M. L. Sui, J. Lu, K. Lu, *Acta Mater.* **2002**, *50*, 4603.
- [27] H. Q. Sun, Y. N. Shi, M. X. Zhang, K. Lu, *Acta Mater.* **2007**, *55*, 975.
- [28] L. Wagner, *Mater. Sci. Eng., A* **1999**, *263*, 210.
- [29] X. Wang, Y. S. Li, Q. Zhang, Y. H. Zhao, Y. T. Zhu, *J. Mater. Sci. Technol.* **2017**, *33*, 758.

- [30] J.-S. Li, W.-D. Gao, Y. Cao, Z.-W. Huang, B. Gao, Q.-Z. Mao, Y.-S. Li, *Adv. Eng. Mater.* **2018**, *20*, 1800402.
- [31] Z. Huang, Y. Cao, J. Nie, H. Zhou, Y. Li, *Materials* **2018**, *11*, 366.
- [32] Y. Li, L. Li, J. Nie, Y. Cao, Y. Zhao, Y. Zhu, *J. Mater. Res.* **2017**, *32*, 4443.
- [33] Y. Cao, Y. B. Wang, X. Z. Liao, M. Kawasaki, S. P. Ringer, T. G. Langdon, Y. T. Zhu, *Appl. Phys. Lett.* **2012**, *101*, 231903.
- [34] Y. L. Wei, A. Godfrey, W. Liu, Q. Liu, X. Huang, N. Hansen, G. Winther, *Scr. Mater.* **2011**, *65*, 355.
- [35] N. Hansen, *Scr. Mater.* **2004**, *51*, 801.
- [36] T. Yu, D. A. Hughes, N. Hansen, X. Huang, *Acta Mater.* **2015**, *86*, 269.
- [37] M. Kawasaki, Z. Horita, T. G. Langdon, *Mater. Sci. Eng., A* **2009**, *524*, 143.
- [38] K. Edalati, Z. Horita, *Acta Mater.* **2011**, *59*, 6831.
- [39] A. Belyakov, K. Tsuzaki, H. Miura, T. Sakai, *Acta Mater.* **2003**, *51*, 847.
- [40] R. B. Figueiredo, T. G. Langdon, *Mater. Sci. Eng., A* **2009**, *501*, 105.
- [41] K. Edalati, Z. Horita, *Mater. Sci. Eng., A* **2011**, *528*, 7514.
- [42] K. Edalati, J. M. Cubero-Sesin, A. Alhamidi, I. F. Mohamed, Z. Horita, *Mater. Sci. Eng., A* **2014**, *613*, 103.
- [43] J. J. Gracio, *Mater. Sci. Eng., A* **1995**, *196*, 97.
- [44] Q. Liu, X. Huang, D. J. Lloyd, N. Hansen, *Acta Mater.* **2002**, *50*, 3789.
- [45] K. Lu, *Science* **2014**, *345*, 1455.
- [46] J. Gu, L. Zhang, S. Ni, M. Song, *Micron* **2018**, *105*, 93.
- [47] X. L. Wu, P. Jiang, L. Chen, J. F. Zhang, F. P. Yuan, Y. T. Zhu, *Mater. Res. Lett.* **2014**, *2*, 185.
- [48] X. Wu, Y. Zhu, *Mater. Res. Lett.* **2017**, *5*, 527.
- [49] E. Ma, T. Zhu, *Mater. Today* **2017**, *20*, 323.